


An exact dual-integral formulation of the indentation of finite, free-standing, end-supported adhesive elastic layers

Mathematics and Mechanics of Solids
1–26
© The Author(s) 2018
Reprints and permissions:
sagepub.co.uk/journalsPermissions.nav
DOI: 10.1177/1081286518786069
journals.sagepub.com/home/mms


Venugopala Swami Punati

Mechanics & Applied Mathematics Group, Department of Mechanical Engineering, Indian Institute of Technology Kanpur, Kanpur, Uttar Pradesh, India

Ishan Sharma

Mechanics & Applied Mathematics Group, Department of Mechanical Engineering, Indian Institute of Technology Kanpur, Kanpur, Uttar Pradesh, India

Pankaj Wahi

Mechanics & Applied Mathematics Group, Department of Mechanical Engineering, Indian Institute of Technology Kanpur, Kanpur, Uttar Pradesh, India

Received 21 March 2018; accepted 8 June 2018

Abstract

We study indentation by a rigid cylindrical punch of finite, free-standing, adhesive elastic layers that are supported only at their ends. The adhesion is considered through an adhesive-zone model. Formulating the boundary-value problem, we obtain two coupled Fredholm integral equations of the first kind, which are solved by a collocation method. Results for non-adhesive contact are obtained when adhesion is zero, and they match well with our own finite element computations and earlier approximate analyses. Additionally, we obtain new results for deeper indentation of non-adhesive contact. In the limit of very adhesive and/or very soft solids, we formulate an approximate model similar to the well-known Johnson–Kendall–Roberts (JKR) model for half-spaces. Our results for adhesive contact match well with preliminary indentation experiments on adhesive layers. Finally, we demonstrate the utility of our approach in modelling structural adhesives through a specific example.

Keywords

adhesion, contact mechanics, dual-integral equations, elastic layer, structural adhesive

1. Introduction

Hertz, in 1882, proposed a theory for the contact of non-adhesive elastic spheres, which is easily modified to address the indentation of three-dimensional elastic half-spaces by rigid, axisymmetric punches. Later, Johnson et al. [1], Derjaguin [2] and Derjaguin et al. [3] proposed conflicting theories for adhesive axisymmetric indentation; these are known as, respectively, JKR and DMT approximations. Finally, Maugis [4] employed an adhesive-zone model to demonstrate that both JKR and DMT approximations may be obtained as the two limits

Corresponding author:

Venugopala Swami Punati, Department of Mechanical Engineering, Indian Institute of Technology Kanpur, Kanpur, Uttar Pradesh, India - 208016
Email: punati.iitk@gmail.com

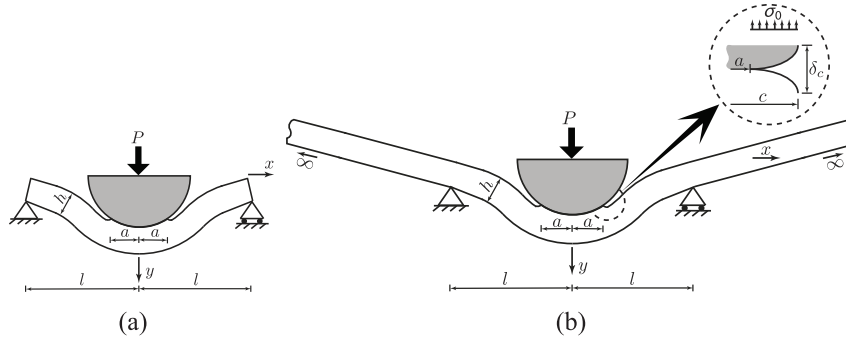


Figure 1. (a) Indentation by a rigid cylindrical punch of a finite, free-standing, adhesive, simply supported elastic layer. (b) Mathematical model for the system in (a) obtained by extending the elastic layer to infinity along its slope near the ends. The inset shows the adhesive-zone model employed in our mathematical formulation.

of a general theory when the strength of the adhesion relative to the stiffness of the elastic substrate grows to infinity or reduces to zero. These theories and their two-dimensional versions are discussed in the literature [5–10].

In recent years, indentation of thin adhesive structures has attracted the attention of researchers because of their applications in the electronics and computer industries, and in biological tissues. At the same time, adhesive layers themselves find applications in other devices/areas: in electronic devices like micro-/nano-electromechanical devices [11, 12]; in the characterization of adhesion of graphene membranes [13–15]; to model de-lamination of elastic layers [16] and the formation of blisters in them [17]; and to understand adhesion mechanisms in geckos [18], which are studied for proper design of grip-and-release adhesives [19]. Modelling and characterization of adhesive layers thus continues to attract great interest [20–22].

The myriad applications above motivates the present investigation into the general problem of the indentation of free-standing, adhesive, elastic layers of finite length that are supported only at their two ends, as shown in Figure 1(a). This, as we will show, constitutes a first step towards the modelling of a variety of structural adhesives.

Previous related studies have considered, at most, indentation of *non*-adhesive beams [23, 24]. These employed, respectively, integral transforms and Fourier series. Recently, Kim et al. [25] revisited the indentation of non-adhesive beams through approximate techniques. However, extending the methods of these papers to an exact analysis of adhesive elastic layers is difficult, as they involve several iterated integral transforms and asymptotic matching with beam theories. In contrast, we address non-adhesive and adhesive contact of elastic layers in an exact manner within the same framework.

For brevity of presentation, we will restrict ourselves to clamped and simply supported adhesive elastic layers. We have shown elsewhere in the context of contact of elastic beams [26] that these two boundary conditions bound the range of behaviours displayed by layers held between flexible end supports.

Adhesion is modelled through an adhesive-zone model following Maugis [4], which is described in the inset of Figure 1(b).

This paper is organized as follows. We first present the mathematical model, which leads to a set of dual-integral equations in terms of two unknowns: the contact pressure and the vertical displacement of the layer's bottom surface. The integral equations are then solved by a collocation technique. We then briefly discuss the finite element (FE) computations that are compared with our results for non-adhesive indentation. Next, we present results for the indentation of clamped and simply supported adhesive and non-adhesive elastic layers. Finally, we compare our predictions with preliminary experiments on adhesive layers and also demonstrate the utility of our approach in modelling real structural adhesives.

2. Mathematical model

We wish to investigate indentation of free-standing finite layers of the type shown in Figure 1(a). The length of the layer is $2l$. It is found cumbersome mathematically to work with layers of finite extent. We, therefore, replace (mathematically) the finite layer by an *infinite* layer by extending the layer of Figure 1(a) beyond the supports to infinity, as shown in Figure 1(b). This extension is done in a manner consistent with the kinematic and kinetic

constraints imposed by the supports. Thus, finite layers are extended linearly along their slope at the supports, thereby maintaining continuity of displacement and slope. The extended linear elastic layer of infinite length in Figure 1(b) has thickness h , Young's modulus E and Poisson's ratio ν , and is supported at only two points that are $2l$ apart. The layer's top and bottom surfaces are taken to be frictionless.

The layers are indented by a rigid, cylindrical punch of radius R subjected to a load P . The punch subsequently moves down by δ and makes contact with the layer over a length $2a$. The applied load P exerts the traction $P_c(x)$ on the layer, which includes both the interaction pressure $p(x)$ in contact area $|x| \leq a$ and the traction σ_0 in the adhesive zone $a \leq |x| \leq c$. During indentation, the vertical displacement of the layer's bottom surface is $v_b(x)$. The work of adhesion between the punch and the adhesive layer is w .

We first set $\chi = x/l$ and $\gamma = h/l$. We rescale x, y, c, l and h by the contact area a , but do *not* rename them, so that the contact patch now lies within $x = -1$ and $x = 1$. We then introduce the following non-dimensional parameters:

$$\begin{aligned} \{\Phi_c(x), \varphi(x)\} &= \frac{a}{\pi w} \{P_c(x), p(x)\}; \quad \bar{P} = \frac{P}{\pi w}; \\ \Delta &= \delta \left(\frac{K^2}{\pi^2 w^2 R} \right)^{1/3}; \quad \lambda = 2\sigma_0 \left(\frac{R}{\pi w K^2} \right)^{1/3}; \\ A &= a \left(\frac{K}{\pi w R^2} \right)^{1/3}; \quad m = \left(\frac{\pi w}{RK} \right)^{1/3}, \end{aligned} \quad (1)$$

where $K = 4E/3(1 - \nu^2)$. The air-gap between the punch and the layer and the vertical displacements of the layer's top and bottom surface will be scaled as δ . The normal traction $\sigma_{yy}(x, h)$ on the bottom surface ($y = h$) of the layer is scaled by $(8\gamma/3KL)$. In the subsequent development, x and χ locate material points on, respectively, the layer's top and bottom surface.

To resolve the contact problem, we need to solve for two unknowns: the interaction pressure $\varphi(x)$ and the bottom surface's vertical displacement $v_b(\chi)$. These are obtained as the solution to the coupled integral equations:

$$\begin{aligned} \Delta - \frac{1}{2}x^2A^2 &= -\frac{8m}{3\pi} \int_0^\infty \bar{\varphi} \left(\frac{\omega}{h} \right) K_1^t \left(\frac{\omega}{h}, x \right) d\omega \\ &\quad - \frac{8\lambda A}{3\pi} \int_0^\infty \bar{\varphi}_0 \left(\frac{\omega}{h} \right) K_1^t \left(\frac{\omega}{h}, x \right) d\omega \\ &\quad + \frac{1}{\pi\gamma} \int_0^\infty \bar{v}_b \left(\frac{\omega}{\gamma} \right) K_2^t \left(\frac{\omega}{h}, x \right) d\omega \quad \text{for } -1 \leq x \leq 1 \end{aligned} \quad (2)$$

and

$$\begin{aligned} 0 &= -\frac{8m}{3\pi} \int_0^\infty \bar{\varphi} \left(\frac{\omega}{h} \right) K_1^b \left(\frac{\omega}{\gamma}, \chi \right) d\omega \\ &\quad - \frac{8\lambda A}{3\pi} \int_0^\infty \bar{\varphi}_0 \left(\frac{\omega}{h} \right) K_1^b \left(\frac{\omega}{\gamma}, \chi \right) d\omega \\ &\quad + \frac{\gamma}{\pi} \int_0^\infty \bar{k}_b \left(\frac{\omega}{\gamma} \right) K_2^b \left(\frac{\omega}{\gamma}, \chi \right) d\omega \quad \text{for } -1 < \chi < 1, \end{aligned} \quad (3)$$

where the overbar indicates the Fourier transform of the function, the *curvature* $\kappa_b = d^2v_b/d\chi^2$, $\omega = \xi h$, and the kernels

$$\begin{aligned} K_1^t\left(\frac{\omega}{h}, x\right) &= \frac{\sinh^2 \omega}{\omega(\omega + \sinh \omega \cosh \omega)} \cos\left(\frac{\omega x}{h}\right), \\ K_2^t\left(\frac{\omega}{h}, x\right) &= \frac{\sinh \omega + \omega \cosh \omega}{\omega + \sinh \omega \cosh \omega} \cos\left(\frac{\omega x}{h}\right), \\ K_1^b\left(\frac{\omega}{\gamma}, \chi\right) &= \frac{\sinh \omega + \omega \cosh \omega}{\omega + \sinh \omega \cosh \omega} \cos\left(\frac{\omega \chi}{\gamma}\right) \\ \text{and } K_2^b\left(\frac{\omega}{\gamma}, \chi\right) &= \frac{\sinh^2 \omega - \omega^2}{\omega(\omega + \sinh \omega \cosh \omega)} \cos\left(\frac{\omega \chi}{\gamma}\right). \end{aligned} \quad (4)$$

We provide below a summary of the steps leading to equations (2) and (3), and details are available in Appendix A:

1. We first Fourier transform [27] the plane-strain, two-dimensional elasticity equations governing Figure 1(b). This yields the vertical displacement $v(x, y = 0)$ of the layer's top surface in terms of integrals over the top and bottom surfaces of, respectively, the traction $\Phi_c(x)$ on the top surface and the displacement $v_b(\chi)$ of the bottom surface. A similar equation is found for the normal traction $\sigma_{yy}(x, h)$ on the layer's bottom surface. These two equations are of the form (2) and (3), respectively. They are now simplified using conditions of contact.
2. The traction $\Phi_c(x)$ and displacement $v_b(\chi)$ are *not* known for all x and χ . Instead, displacement and traction are prescribed in some regions of the top and bottom surfaces, respectively. The punch's profile dictates the vertical displacement of the top surface in the contact zone, and the bottom surface is free of traction between $\chi = -1$ and $\chi = 1$. Thus,

$$v(x, 0) = \Delta - \frac{1}{2}x^2A^2 \quad \text{for } -1 \leq x \leq 1, \quad (5)$$

$$\text{and } \sigma_{yy}(\chi, h) = 0 \quad \text{for } -1 < \chi < 1, \quad (6)$$

where Δ is the punch's displacement, and we have assumed $\delta \ll R$. The above equations lead to the left-hand sides of equations (2) and (3).

3. The adhesive interaction between the punch and the layer is assumed to follow the Dugdale–Barenblatt adhesive-zone model [4]. In this model, a *constant* normal traction σ_0 acts per unit length within the adhesive zone. The adhesive zone is of length $d = c - 1$, where c demarcates the zone's outer edge; see the inset in Figure 1(b). With this, we write the *non-dimensional* normal traction on the top surface as

$$\Phi_c(x) = \begin{cases} \varphi(x) & \text{for } |x| \leq 1, \\ -\lambda A/2m & \text{for } 1 \leq |x| \leq c, \\ 0 & \text{for } |x| > c. \end{cases} \quad (7)$$

When introduced into the Fourier-transformed equations of step (1), the above leads to the right-hand sides of equations (2) and (3). We note that the total load on the punch is found by integrating equation (7) from $-c$ to c :

$$\bar{P} = \int_{-1}^1 \varphi(x) dx - \frac{\lambda A}{m}(c - 1). \quad (8)$$

We still require additional conditions to complete the adhesive-zone description of step (3) above. These are now derived.

An adhesive zone introduces the extra variable c into the contact problem. The required additional equation is obtained by equating the energy release rate G – computed employing the J -integral [28] – to the work of adhesion w , to yield the energy balance¹

$$\frac{\pi \lambda}{2} \delta_c = 1, \quad (9)$$

where

$$\delta_c = \frac{1}{2}c^2A^2 - \Delta + v_c \quad (10)$$

is the air-gap at the end of the adhesive zone, and $v_c = v(c, 0)$ is the vertical displacement of the top surface at $x = c$; see inset in Figure 1(b). We obtain v_c by evaluating the right-hand side of equation (2) at $x = c$. Next, the adhesive-zone model is introduced to resolve stress singularities at the contact edges ($x = \pm 1$). Thus, we impose continuity of the normal traction at $x = \pm 1$, that is:

$$\lim_{x \rightarrow \pm 1^\mp} \varphi(x) = -\frac{\lambda A}{2m}. \quad (11)$$

The governing equations (2) and (3) are coupled Fredholm integral equations of the first kind [29] that are to be solved along with conditions (9)–(11). This cannot be done analytically due to the complex kernels (4). We will, therefore, implement a numerical solution in the next section. But, first we make two remarks relevant to adhesion-free contact and to a JKR-like approximation that is useful for highly adhesive, soft layers:

1. In *non*-adhesive indentation $\lambda = 0 = w$, and equation (9) is automatically satisfied.
2. When the JKR approximation is invoked, adhesive stresses dominate the material's stiffness, so that $\lambda \rightarrow \infty$. Thus, the adhesive zone is assumed to vanish, that is $c \rightarrow 1$. Then, employing Griffith's criterion² [30], the energy balance (9) becomes

$$\frac{2\pi m^2 K_1^2}{3A} = 1, \quad (12)$$

where

$$K_1 = -\lim_{x \rightarrow 1^-} \sqrt{2\pi(1-x)}\varphi(x) \quad (13)$$

is a *stress intensity factor*. The continuity condition (11) is now redundant.

2.1. Numerical solution

We approximate the contact pressure $\varphi(x)$ and the displacement $v_b(\chi)$ of the layer's bottom surface as, respectively,

$$\varphi(x) = \frac{-\lambda A}{2m} + \frac{1}{\sqrt{(1-x^2)}} \sum_{n=0}^N b_{2n} T_{2n}(x) \quad \text{for } -1 \leq x \leq 1, \quad (14)$$

and

$$v_b(\chi) = d_0 + \sum_{n=1}^M d_n S_n(\chi) \quad \text{for } -1 \leq \chi \leq 1, \quad (15)$$

where $T_{2n}(x)$ are Chebyshev polynomials of the first kind, $S_n(\chi) = \cos(n\pi\chi)$ for a clamped layer and $\sin\{(2n-1)\pi(\chi+1)/2\}$ for a simply supported layer – these are chosen to satisfy end conditions (see Appendix B) – and b_{2n} and d_n are constants that are to be determined. Only even Chebyshev polynomials are considered as the indentation is symmetric. The constant term in equation (14) explicitly accounts for the contact pressure at the contact edge in the adhesive-zone model; see equation (11). The curvature κ_b of the layer is obtained as $d^2 v_b / d\chi^2$. Substituting equation (14) in (2) and inserting equation (15) into (3) leads to $N + 1$

and M algebraic equations, respectively,

$$\begin{aligned} \Delta - \frac{1}{2} x_i^2 A^2 &= \frac{8m}{3\pi} \sum_{n=0}^N b_{2n} \mathcal{J}_{2n}^t(x_i) - \frac{8\lambda A}{3\pi} \mathcal{J}^t(x_i) \\ &+ \frac{1}{\pi \gamma} \sum_{n=1}^M d_n \mathcal{Q}_n^t(x_i) \quad \text{for } i = 1, \dots, N+1 \end{aligned} \quad (16)$$

and

$$\begin{aligned} 0 &= \frac{8m}{3\pi} \sum_{n=0}^N b_{2n} \mathcal{J}_{2n}^b(\chi_k) - \frac{8\lambda A}{3\pi} \mathcal{J}^b(\chi_k) \\ &+ \frac{\gamma}{\pi} \sum_{n=1}^M d_n \mathcal{Q}_n^b(\chi_k) \quad \text{for } k = 1, \dots, M, \end{aligned} \quad (17)$$

where x_i and χ_k are collocation points, and \mathcal{J}^t and \mathcal{Q}_n^t are functions derived from the kernels (4) through projection integrals; the details are given in Appendix C.

Employing the series approximation (equations (14) and (15)) in the constraints (9)–(11) provides

$$\frac{\pi \lambda}{2} \left(\frac{1}{2} c^2 A^2 - \Delta + v_c \right) = 1 \quad (18)$$

and

$$b_0 + b_2 + \dots + b_{2N} = 0. \quad (19)$$

In the JKR approximation, equation (11) replaces (12), so that utilizing equation (14) leads to

$$b_0 + b_2 + \dots + b_{2N} = -\frac{\sqrt{6A}}{2\pi m}, \quad (20)$$

which then takes the place of equation (19). Utilizing equation (14) in (8) yields the total load acting on the punch as

$$\bar{P} = \pi b_0 - \frac{\lambda A c}{m}. \quad (21)$$

Discretizing equations (2) and (3) led to the $N + M + 1$ algebraic equations (16) and (17). Along with the discretized constraints (18) and (19), we finally obtain the $N + M + 3$ equations required to solve for the $N + 1$ unknowns b_{2n} , the M unknowns d_n , Δ and c . We note that the constant d_0 in equation (15) is found by satisfying kinematic conditions at the supports $\chi = \pm 1$. This system of nonlinear algebraic equations is solved for any given contact area A following the algorithm in Appendix C. The results obtained are discussed next.

3. Results

3.1. Non-adhesive contact

We first consider the non-adhesive indentation of clamped and simply supported layers. In the absence of adhesion, we set $\lambda = 0$ in equations (2) and (3). The corresponding discretized forms follow from equations (16) and (17), respectively:

$$\Delta - \frac{1}{2} x_i^2 A^2 = \frac{8\gamma^3}{3\pi} \sum_{n=0}^N b_{2n} \mathcal{J}_{2n}^t(x_i) + \frac{1}{\pi \gamma} \sum_{n=1}^M d_n \mathcal{Q}_n^t(x_i) \quad (22)$$

and

$$0 = \frac{8\gamma^3}{3\pi} \sum_{n=0}^N b_{2n} \mathcal{J}_{2n}^b(\chi_k) + \frac{\gamma}{\pi} \sum_{n=1}^M d_n \mathcal{Q}_n^b(\chi_k). \quad (23)$$

Non-adhesive contacting surfaces detach smoothly, so that the pressure vanishes at the contact edge, and equation (18) holds. We solve equations (22), (23) and (18) through the numerical algorithm of Appendix C. We set $N = 5$ and $M = 50$ in our computations.

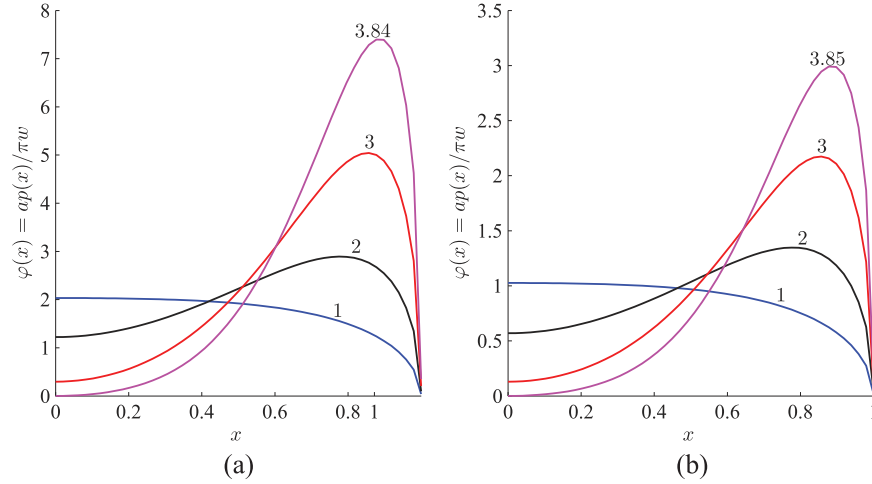


Figure 2. Non-adhesive contact of (a) clamped and (b) simply supported layers. We plot the non-dimensional contact pressures $\varphi(x)$ at several A as noted next to their corresponding curves. We set $h = 4$ mm and $l = 40$ mm.

We present below some new results for the indentation of adhesionless layers. Appendix D compares our results with our FE computations and with approximate theories [23, 24]. In each case, excellent match is found, which validates our approach and helps build confidence in its application to adhesive layers later.

We set Young's modulus, Poisson's ratio and adhesion energy to $E = 0.083$ MPa, $\nu = 0.4$ and $w = 0.02 \times 10^{-3}$ J/mm², respectively, as representative of typical soft adhesives. In the case of non-adhesive contact w serves only to facilitate non-dimensionalization. Other geometric parameters are: $l = 40$ mm, $R = 225$ mm and $h = 4$ mm.

We plot the contact pressure $\varphi(x)$ for several contact areas A in Figure 2. We observe that when A is small, φ is maximum at the centre of the contact patch. With increasing A , the pressure profiles become double-humped and φ reaches its maximum near the contact edges. For $A = 3.84$ (3.85), φ at the centre of the contact patch becomes zero for clamped (simply supported) layers. Increasing the contact area further leads to negative (tensile) pressure at the centre of the contact patch, reflecting loss of contact between the punch and the adhesionless elastic layer. Our formulation has not yet been extended to discontinuous contact areas, so we do not investigate larger A .

We plot the variation of the contact area A with total load \bar{P} acting on the punch and with the punch's displacement Δ at several slenderness ratios l/h in Figure 3. Both clamped and simply supported layers are considered, whose results are found to be qualitatively similar. With increasing l/h the layer's resistance to bending decreases and, hence, we find smaller loads \bar{P} , or larger deflections Δ , at the same contact area A . For the same reason the load \bar{P} required to achieve the same A in simply supported layers is smaller than for clamped layers. At the same time, the displacements Δ are higher in simply supported layers.

In Figure 3, we observe that curves change their slope abruptly, leading to sudden increase in A . This is due to the layer wrapping around the punch rapidly with only a small increase in the load on the punch or in its displacement. This wrapping happens when the profile of the layer's top surface begins to conform with the punch's profile, as shown in Figure 4. As slender layers bend easily, wrapping initiates in such layers at lower loads (Figures 3(a) and (c)) and smaller displacements (Figures 3(b) and (d)).

3.2. Adhesive contact: JKR approximation

A JKR-like approximation is recovered when the scaled adhesive strength $\lambda \rightarrow \infty$ and the adhesive zone vanishes, that is $\bar{c} \rightarrow 1$. In this limit, the discretization of equations (2) and (3) continues to be given by, respectively, equations (22) and (23). The condition on the contact pressure at $x = \pm a$ is determined by Griffith's criterion (equation (20)). We now solve equations (22), (23) and (20) following the algorithm of Appendix C.

We first plot contact stresses $\varphi(x)$ for several contact areas A in Figure 5. We observe that φ is negative (tensile) and singular at contact edges, which is typical of the JKR approximation. As in Section 3.1, with increasing A the maximum compressive contact stresses are found near the contact edges and a double-humped profile is observed. For high A , φ becomes negative (tensile) at the centre of the contact area. The region over

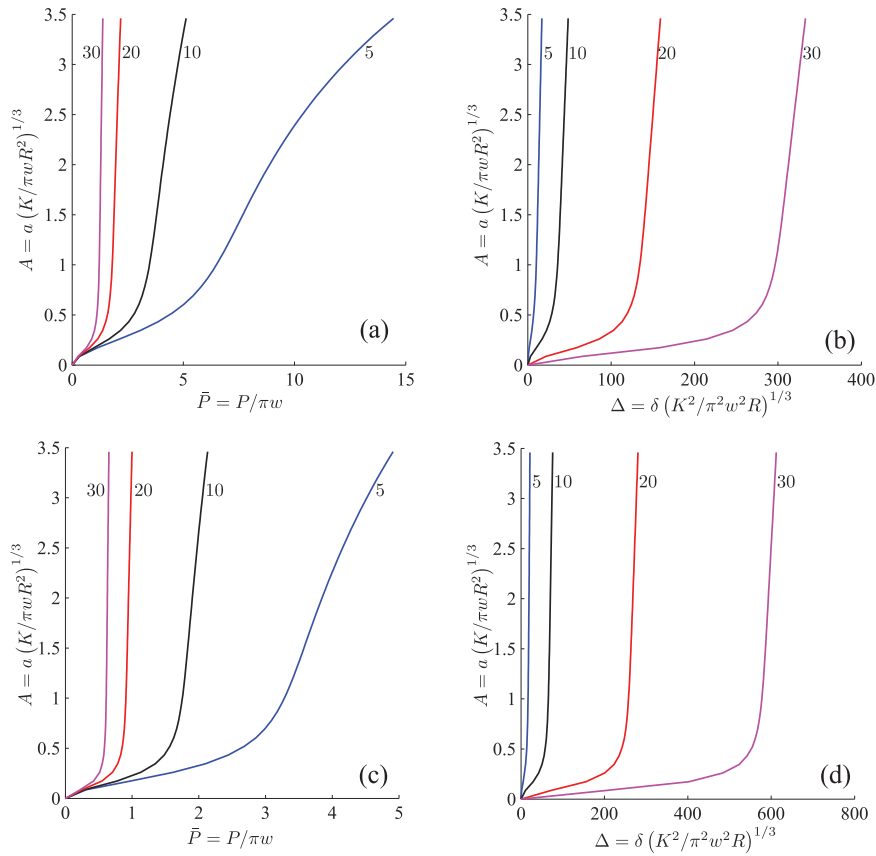


Figure 3. Non-adhesive contact of clamped (top row) and simply supported (bottom row) layers. Variation of contact area A with total load \bar{P} (left column) and the punch's displacement Δ (right column) is shown. Several slenderness ratios l/h are considered and these are noted next to their associated curves.

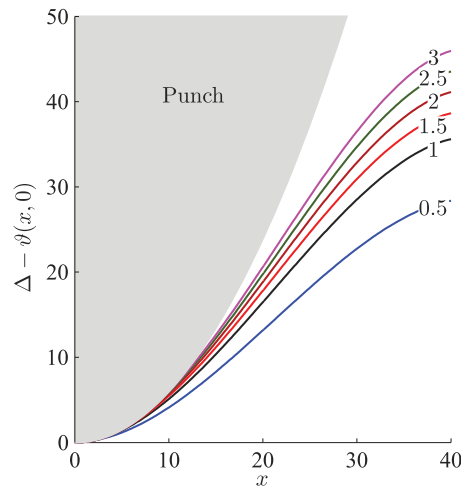


Figure 4. Non-adhesive contact of a clamped layer. We plot the non-dimensional displacement $\Delta - v(x, 0)$ with respect to the cylindrical punch of the layer's top surface. Several A are investigated as noted next to the curves. We set $h = 4$ mm and $l = 40$ mm.

which this tensile stress acts also increases by increasing A ; see inset in Figure 5. Moreover, multiple regions of tensile stresses are also seen; see $A = 7$ curve in the inset of Figure 5(b). The presence of negative φ , however, does *not* indicate contact separation as tensile stresses are admitted in the JKR approximation, and are supposed to reflect adhesive interaction. Finally, comparing Figures 5(a) and (b), we find that, as expected, much less pressure is required in simply supported layers to achieve the same contact area.

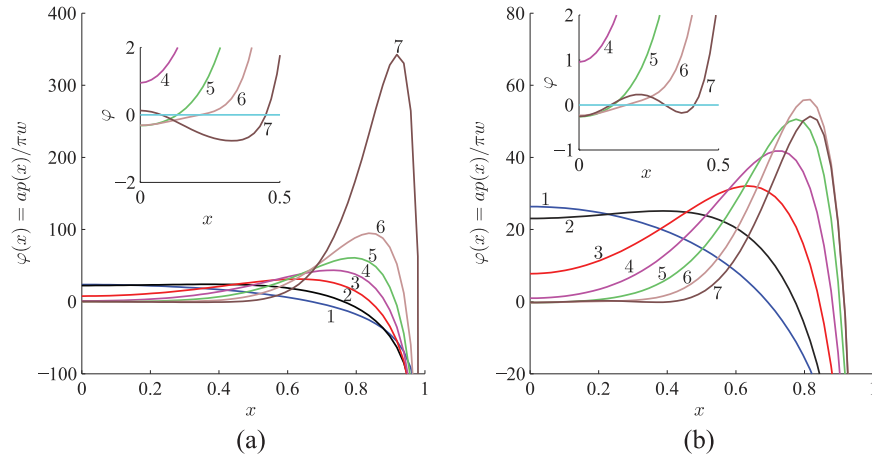


Figure 5. Adhesive contact of (a) clamped and (b) simply supported layers with the JKR approximation. We plot the contact pressures $\varphi(x)$ at several A whose values are noted next to their corresponding curves. We set $h = 4$ mm and $l = 20$ mm. The insets show the pressure profiles at lower values of x . We note that $\varphi \rightarrow -\infty$ as $x \rightarrow 1$, which is typical of the JKR approximation. For high A , φ is negative, that is tensile, at the centre of the contact area, and in multiple regions when $A = 7$ for a simply supported layer.

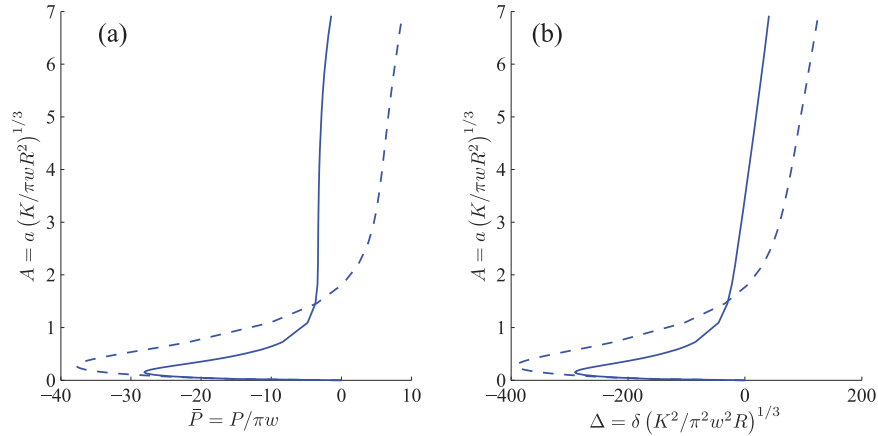


Figure 6. Adhesive contact of clamped layers with the JKR approximation. Variation of contact area A with (a) total load \bar{P} and (b) the punch's displacement Δ is shown. The layer's slenderness ratio $l/h = 10$. The solid line corresponds to $l = 40$ mm and $h = 4$ mm, while the dashed line is for a layer with $l = 80$ mm and $h = 8$ mm.

In Figure 6 we plot the variation of the contact area A with the load \bar{P} acting on the punch and the displacement Δ of the punch for clamped layers. The slenderness ratio l/h is kept constant, but two different combinations of l and h are investigated. We observe that the response of the layer is sensitive to l and h individually, and *not* on the slenderness ratio alone. The results for simply supported layers are qualitatively similar.

Results in Figure 7 are obtained for several l/h by varying l while keeping $h = 4$ mm. However, the results are qualitatively similar in many respects to those obtained by varying h . Layers with high l/h bend easily under the influence of adhesion, and we observe smaller negative loads \bar{P} and larger negative displacements Δ at a given contact area A . Negative loads and displacements indicate, respectively, *downward* force on the punch and the upward bending of layers. From Figure 7 we again observe that slender layers wrap around the punch earlier, that is at smaller \bar{P} , as indicated by the sudden changes in the slope in $A-\bar{P}$ and $A-\Delta$ curves in Figure 7. For sufficiently slender layers (e.g. the curves for $l/h = 20$ in Figure 7), wrapping occurs even when there is no net compressive (positive) load on the punch. In these very flexible layers, bending resistance is unable to even counterbalance adhesive forces. Such adhesive layers have MEMs/NEMs applications [11, 12]. Finally, from Figures 7(a) and (b), for $l/h=5$, we observe that at high A the load response increases abruptly. This is due to the influence of the end supports on the contact area. The above features, namely extent of wrapping

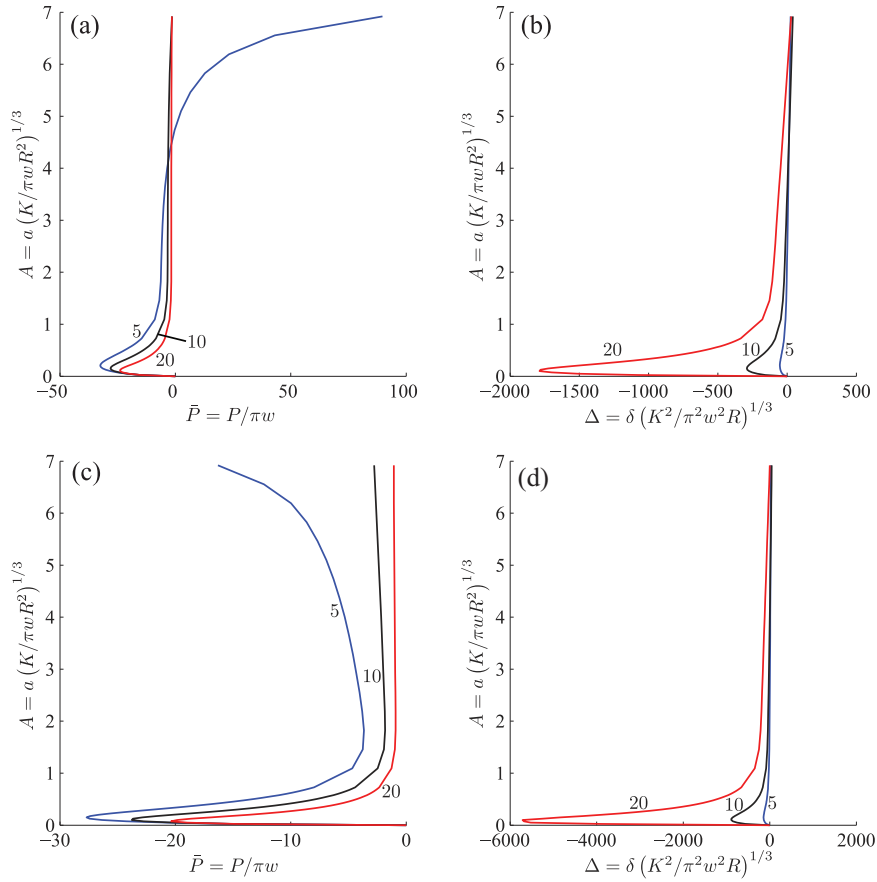


Figure 7. Adhesive contact of clamped (top row) and simply supported layers (bottom row) with the JKR approximation. Variation of contact area A with total load (left column) \bar{P} and the punch's displacement Δ (right column) is shown. Results are obtained for several values of l/h , as noted next to their corresponding curves, while keeping $h = 4$ mm.

and the response to adhesive forces, are, expectedly, heightened in the case of simply supported layers, whose bending resistance is smaller.

From Figure 7(c) we observe that, for $A \gtrsim 1.5$, in a simply supported layer of $l/h = 5$, the load \bar{P} decreases with increase in contact area A . At the same time, the punch's displacement Δ increases; see the inset in Figure 7(d). This anomalous behaviour is explained by the presence of negative (tensile) stresses at the centre of the contact region in addition to the very large negative stresses at the contact edges. The contact region over which these tensile stresses act also grows with increase in contact area; see Figure 5. Because of this the net force on the punch may start to decrease at large A , as is observed when $l/h = 5$.

3.3. Adhesive contact with an adhesive-zone model

Finally, we study the indentation of adhesive layers with the help of adhesive-zone models. In these models an adhesive force acts over an adhesive zone of length $d = c - a$ outside the contact area. The distribution of the adhesive forces follows the Dugdale–Barenblatt model [4], and the normal traction on the layer's top surface is given by equation (7). The contact problem is resolved by solving equations (16)–(19) following the algorithm of Appendix C.

We plot the contact pressure φ for different adhesive strengths λ in Figure 8. We observe that the contact stresses are tensile at the contact edges, and remain constant at $-\lambda A/2m$ over the adhesive zone. With increasing λ , the contact stress distribution in Figure 8 approaches that of the JKR approximation in Figure 5. We also see in Figure 8 that the adhesive zone shrinks outside the contact area. For example, as shown in Figure 8, the pressure profile for $\lambda = 3$ matches closely that obtained through the JKR approximation of Section 3.2.

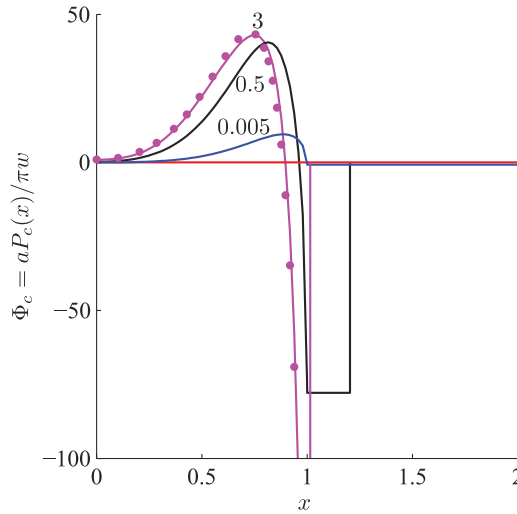


Figure 8. Adhesive contact of clamped layers with an adhesive-zone model. We plot the non-dimensional contact pressures $\varphi(x)$ at $A = 4$ for several adhesive strengths λ that are noted next to their corresponding curves. We set $h = 4$ mm and $l = 40$ mm. Filled circles represent results from the JKR approximation of Section 3.2.

For brevity we investigate the effect of only the adhesive strength λ (see equation (1)) at a given l and h . The response to varying l/h is found to be similar to what was observed in Section 3.2. In Figure 9 we plot the variation of the contact area A with the total load \bar{P} and the displacement Δ for several adhesive strengths λ . We observe that, as $\lambda \rightarrow 0$, the results approach those obtained for non-adhesive indentation discussed in Section 3.1. At the same time, increasing adhesive strength pushes our results towards those obtained for the JKR approximation in Section 3.2.

Next, we study the effect of adhesive strength λ on the adhesive zone's size $d = c - 1$. For this we plot d by varying A for several λ in Figure 10(a). We observe that with increasing λ , d goes rapidly to zero. At high λ the adhesive zone is small, and such cases may be addressed adequately through the JKR approximation of Section 3.2. Finally, as seen in Figure 10(b), varying the geometric parameters of the layer, as well as the type of end supports, does *not* affect the adhesive zone's size significantly, which depends most crucially on λ .

4. Experiments and applications

In this final section, we compare our theoretical predictions with preliminary experiments on a clamped adhesive layer, as well as demonstrate the ability of our theoretical methods to model structural adhesives.

4.1. Experiments

Punati et al. [26] experimentally investigated the indentation of a clamped PDMS (poly-dimethyl-siloxane) layer by a cylindrical glass punch. To make PDMS samples, a uniform mixture of Sylgard 184 silicone elastomer base and curing agent is prepared by taking them in 10:1 weight ratio. Air is desiccated from this mixture, which is then poured into a rectangular mould of desired size. This is cured at room temperature ($\approx 24^\circ\text{C}$) for two days and the PDMS sample is extracted from the mould.

Micro-tensile tests were carried out on PDMS samples, and JKR indentation tests (Figure 11(a)) were performed on thick ($h \approx 25$ mm) PDMS samples. Young's modulus E of PDMS was found to be in the range of 1–2 MPa while, following Chaudhury et al. [31], the work of adhesion $w \approx 27$ mJ/m². These values compare well with those reported earlier in the literature [32, 33]. Figure 11(b) shows the fit of the a - P curve predicted by JKR theory with our experimental data.

We then carried out contact mechanics experiments on a clamped PDMS layer with half-span and thickness maintained at $l \approx 50$ mm and $h \approx 8$ mm, respectively, as shown in Figure 11(a). The total load P and contact patch width $2a$ were measured. The results obtained were then compared with the predictions of the analysis of Section 3.2 in Figure 11(b). We find very good agreement. We observe that the results for a layer vary

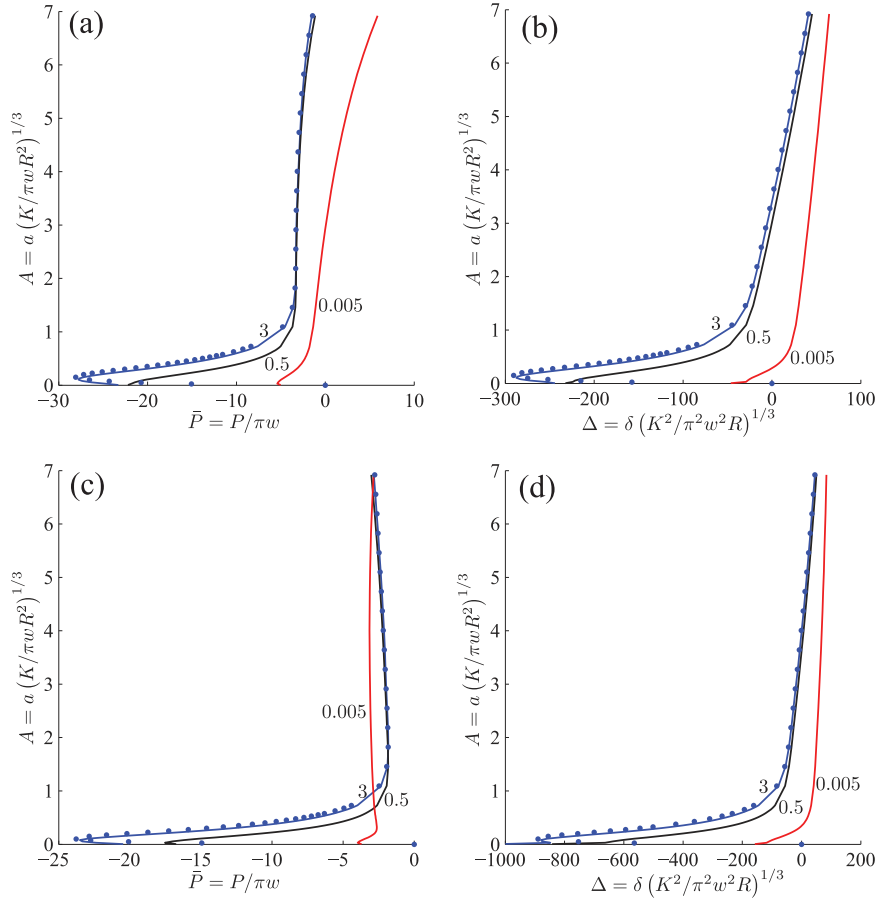


Figure 9. Adhesive contact of clamped (top row) and simply supported (bottom row) layers with an adhesive-zone model. Variation of contact area A with total load \bar{P} (left column) and punch's displacement Δ (right column) is shown. Different adhesive strengths λ are considered and these are indicated next to their associated curves. The layer's thickness $h = 4$ mm and half-span $l = 40$ mm. Filled circles represent the JKR solution for the corresponding layer; see Section 3.2

considerably from that of a half-space, lending support to the necessity for a separate theoretical development for adhesive elastic layers, as presented here.

Finally, we compare our results for adhesive, free-standing layers with those due to more approximate approaches [26]. We consider several geometric and material parameters for the layers and plot variation of the total load P with punch displacement δ in Figure 12. From Figure 12(a), we observe that with decreasing l/h approximate theories are erroneous. This is because Punati et al. [26] estimated the vertical displacement of the layer's bottom surface by replacing the distributed interaction pressure on the layer's top surface by a point load. This approach fails when the layer's thickness is such that contact deformations are accommodated locally and not in the layer's global deformation. Indeed, the inset in Figure 12(a) shows that the vertical displacements of the layer's top and bottom surfaces are consistently lower when we follow the approximate approach [26]. This translates into the layer displaying higher stiffness. Similarly, in Figure 12(b), we show the effect of adhesion energy w on the $P - \delta$ response for a layer with $h = 0.3$ mm. We find that the approximation of Punati et al. [26] fails for all w . Combined with the observation of Figure 11 that layers with $l/h \leq 2$ can be approximated by half-spaces, the comparisons of Figure 12 suggest that in applications with $2 \leq l/h \leq 3.3$, the more exact formulation of the current work should be employed.

More thorough indentation experiments on adhesive elastic layers, where we vary parameters like flexibility of end supports, layers thickness h and the work of adhesion w are in progress.

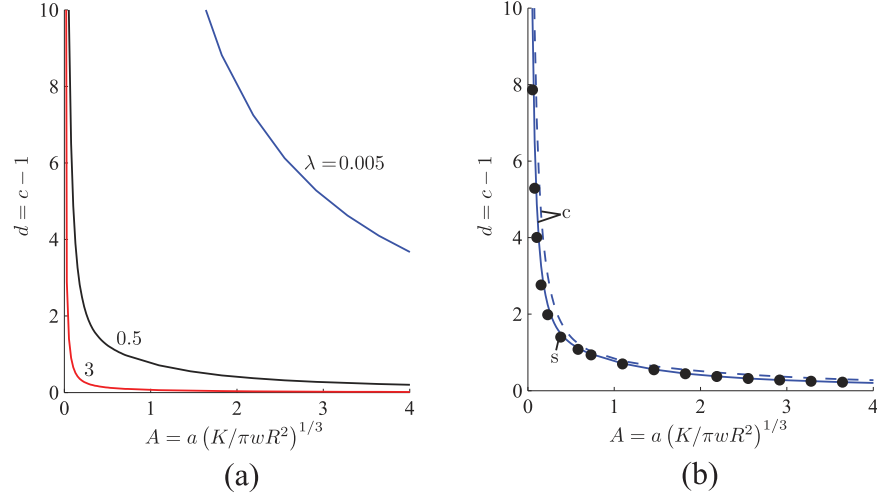


Figure 10. (a) Variation of the adhesive zone size d with the the contact area A at different adhesive strengths λ for a clamped layer. We set $l = 40$ mm and $h = 4$ mm. (b) Variation of the adhesive zone size d with the contact area A for clamped ('c') and simply supported ('s') layers when $\lambda = 0.5$. Solid and dashed lines are the predictions of the clamped layer with $h = 4$ mm, $l = 40$ mm, and $h = 8$ mm, $l = 80$ mm, respectively, while the filled circles indicate results obtained for a simply supported layer with $h = 4$ mm, $l = 40$ mm.

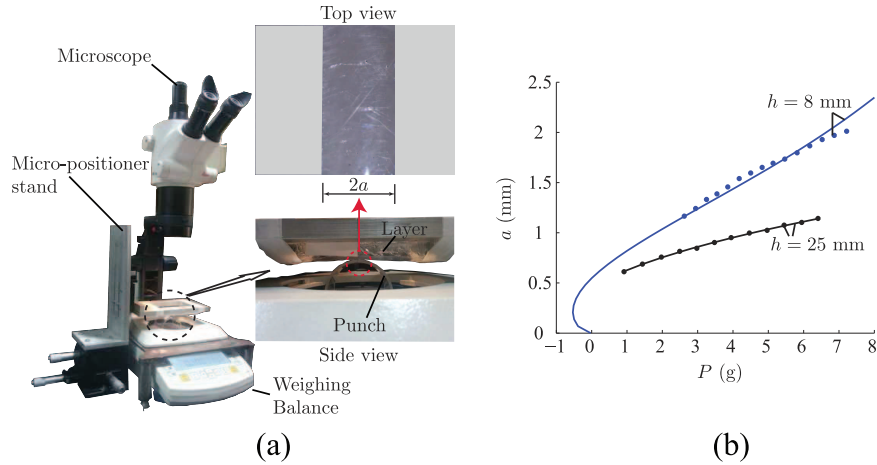


Figure 11. (a) Indentation experiments on PDMS layers. The layers are rigidly attached to the micro-positioner and a cylindrical glass punch of radius $R \approx 27.5$ mm is placed on top of the semi-micro balance. The layers are brought into contact with the glass punch using the micro-positioner. The rectangular contact patch is observed through a microscope to note the contact width a , and the load P acting on the punch is noted from the semi-micro balance. Insets show a close-up of the side view of the indentation and a top view of the contact patch. (b) Variation of the contact area a (in mm) with the total load P (in g). Filled circles represent experimental data. Solid lines correspond to theoretical predictions. For $h = 8$ mm we followed Section 3.2, while for $h = 25$ mm we employed the standard JKR formula for a half-space [31].

4.2. Application

We now demonstrate the utility of our semi-analytical procedure in modelling structural adhesives with one micro-channel developed by Arul and Ghatak [33], shown in Figure 13(a). We employ the parameters shown in Table 1. The stiffnesses of the flexible end supports are estimated from a strength-of-materials approach to be $k_s^f \approx 12b'l^3/h_ch^3$ and $k_t^f \approx lb'^3/h_ch^3$, where the geometrical parameters are indicated in Figure 13(a). We have assumed $b' > h$, as b' is not reported by Arul and Ghatak [33].

We compare our results for clamped and simply supported layers with the experiments of Arul and Ghatak [33] in Figure 13(b). The adhesive strength of the PDMS used in the experiments [33] was such that the JKR

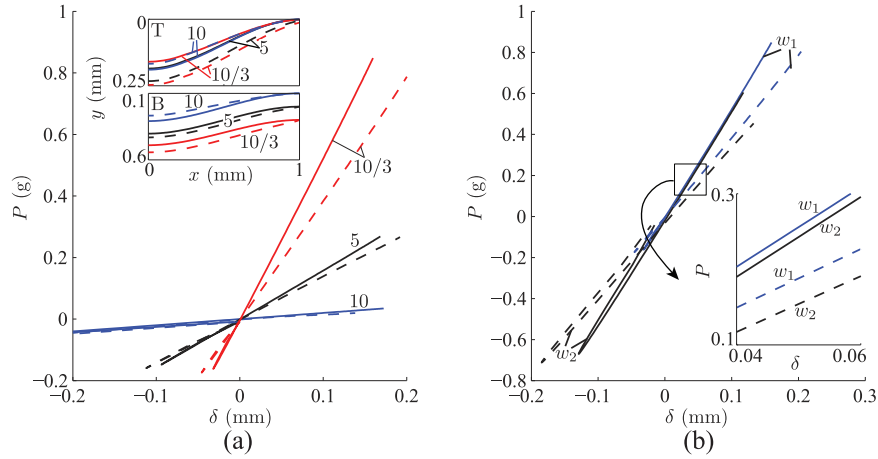


Figure 12. Adhesive contact of clamped layer with JKR approximation. The layer has $l = 1$ mm, $R = 1.1$ mm and $E = 1$ MPa. Solid lines represent results of the approximate procedure (section 7 in Punati et al. [26]), while the dashed lines are predictions from Section 3.2. Variation of the total load P with the punch's displacement δ is shown by varying (a) the layer's thickness h and (b) the work of adhesion w . In (a), three different slenderness ratios l/h are considered as noted next to their curves after setting $w = 27$ mJ/m², while in (b) we set $l/h = 10/3$ and investigate two adhesion values: $w_1 = 27$ mJ/m² and $w_2 = 270$ mJ/m². The insets in (a) represent the y coordinate of the layer's top (T) and bottom (B) surfaces during the indentation when $a = 0.25$ mm.

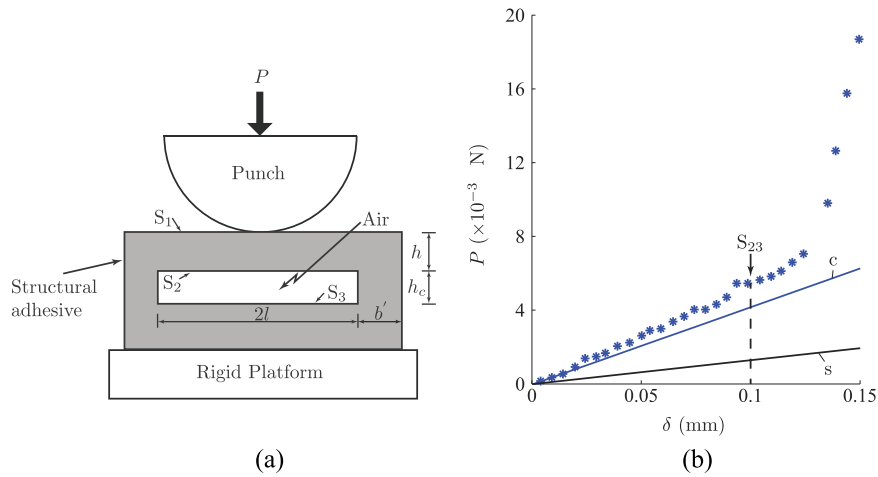


Figure 13. (a) A structural adhesive with one micro-channel. (b) Variation of the total load P with the punch's displacement δ . The solid lines represent solutions obtained from the procedure of Section 3.2, with 'c' and 's' indicating clamped and simply supported layers, respectively. Asterisks (*) are the experimental results of Arul and Ghatak [33].

Table 1. Geometrical and material parameters considered for modelling adhesives with one micro-channel; see also Figure 13(a).

Geometrical and material parameters	Value [33]
Layer thickness	$h = 0.8$ mm
Micro-channel's thickness	$h_c = 0.1$ mm
Layer's length	$2l = 5-8$ mm
Punch radius	$R = 2.24$ mm
Punch length	$l_p = 2.7$ mm
Shear modulus	$G = 1$ MPa
Poisson's ratio	$\nu = 0.49$
Young's modulus	$E = 2(1 + \nu) \approx 3$ MPa
Work of adhesion	$w = 45 \times 10^{-6}$ N/mm

approximation could be invoked [34]. Thus, we follow the procedure of Section 3.2 to generate theoretical predictions. We find good agreement of our results for a *clamped* layer with experiments up to an indentation depth $\delta \approx 0.1$ mm, that is until the point S_{23} . At this point, the bottom surface S_2 begins to interact with the surface S_3 in experiments; see Figure 13(a). This feature is not yet implemented in our mathematical model, so it is expected that our predictions will deviate from the experimental observations once surfaces S_2 and S_3 touch. It is important to note that the results obtained for a simply supported layer do *not* match experiments well in Figure 13(b). This again underscores the role played by the layer's supports in the indentation process, so they need to be modelled carefully.

5. Conclusions

We investigated the indentation of finite, free-standing adhesive elastic layers by solving two coupled Fredholm integral equations of the first kind for the contact pressure p and the displacement v_b of the bottom surface. These equations were solved through a collocation technique employing series approximations for p and v_b . We then compared our results for non-adhesive indentation with our FE simulations and previously published results, and found a satisfactory match. New results about non-adhesive indentation were then presented. Next, we investigated adhesive contact of layers when the JKR approximation is invoked and when an adhesive-zone model is utilized. We then compared theoretical predictions with our preliminary experiments on a clamped adhesive layer and found a very good match. Finally, we showed the utility of our approach to model structural adhesives developed by Arul and Ghatak [33]. The two experimental comparisons demonstrated the importance of including both the layer-like behaviour³ of structural adhesives in theoretical models, as well as correctly modelling the free-standing layer's end supports.

We are presently pursuing extensive experiments on the indentation of free-standing adhesive layers. In the future we aim to extend the present approach to three-dimensional, axisymmetric indentation. By suitably modifying the top and bottom boundary conditions in our theoretical formulation we may also study the adhesion characteristics of graphene membranes in MEMS/NEMS, delamination of elastic layers and grip-and-release processes.

Acknowledgements

We thank Dr T. Bhuvana, Prof. P. Venkitanarayanan and Prof. S.L. Das of the Department of Mechanical Engineering, IIT Kanpur, for help with experiments. We are also grateful to Prof. Akash Anand from the Department of Mathematics and Statistics, IIT Kanpur for useful discussions.

Funding

The author(s) declared the following potential conflicts of interest with respect to the research, authorship, and/or publication of this article: This work received partial financial support from the Department of Mechanical Engineering, IIT Kanpur. V.S. Punati also thanks the Ministry of Human Resource Development, Government of India, for financial support.

Notes

1. In dimensional form, energy balance is given by $\sigma_0 \delta_c = w$.
2. In dimensional form, Griffith's criterion is the equation $K_1^2/2E^* = w$.
3. Rather than modelling these structures as films on a substrate or as half-spaces.

References

- [1] Johnson, KL, Kendall, K, and Roberts, AD. Surface energy and the contact of elastic solids. *Proc R Soc Lond, A* 1971; 324(1558): 301–313.
- [2] Derjaguin, BV. Untersuchungen über die reibung und adhäsion, IV. *Koll Z* 1934; 69(N2): 155–164.
- [3] Derjaguin, BV, Muller, VM, and Toporov, YP. Effect of contact deformations on the adhesion of particles. *J Colloid Interface Sci* 1975; 53(2): 314–326.
- [4] Maugis, D. Adhesion of spheres: the JKR–DMT transition using a Dugdale model. *J Colloid Interface Sci* 1992; 150(1): 243–269.
- [5] Alexandrov, A, and Pozharskii, D. *Three-dimensional contact problems*. Dordrecht: Kluwer Academic Publishers, 2001.
- [6] Galin, LA, and Gladwell, GML. *Contact problems: the legacy of L.A. Galin*. Amsterdam: Springer, 2008.

- [7] Gladwell, GML. *Contact problems in the classical theory of elasticity*. Alphen aan den Rijn: Sijthoff & Noordhoff Publishers, 1980.
- [8] Johnson, KL. *Contact mechanics*. Cambridge: Cambridge University Press, 1985.
- [9] Hills, DA, Nowell, D, and Sackfield, A. *Mechanics of elastic contacts*. Oxford: Butterworth-Heinemann, 1993.
- [10] Goryacheva, IG. *Contact mechanics in tribology*. Amsterdam: Springer, 1998.
- [11] Wagner, TJ, and Vella, D. The sensitivity of graphene “snap-through” to substrate geometry. *Appl Phys Lett* 2012; 100(23): 233111.
- [12] Hu, D, and Adams, GG. Adhesion of a micro-/nano-beam/plate to a sinusoidal/grooved surface. *Int J Solids Struct* 2016; 99: 40–47.
- [13] Koenig, SP, Boddeti, NG, Dunn, ML, et al. Ultrastrong adhesion of graphene membranes. *Nat Nanotechnol* 2011; 6(9): 543–546.
- [14] Huang R. Graphene: show of adhesive strength. *Nat Nanotechnol* 2011; 6(9): 537–538.
- [15] Zhang, Z, and Li, T. Determining graphene adhesion via substrate-regulated morphology of graphene. *J Appl Phys* 2011; 110(8): 083526.
- [16] Wagner, TJ, and Vella, D. Floating carpets and the delamination of elastic sheets. *Phys Rev Lett* 2011; 107(4): 044301.
- [17] Wagner, TJ, and Vella, D. The ‘sticky elastica’: delamination blisters beyond small deformations. *Soft Matter* 2013; 9(4): 1025–1030.
- [18] Sekiguchi, Y, Hemthavy, P, Saito, S, et al. Adhesion between side surface of an elastic beam and flat surface of a rigid body. *J Adhesion Sci Technol* 2012; 26(23): 2615–2626.
- [19] Sekiguchi Y, Lei L, Hemthavy P, et al. Mechanisms for grip-and-release process of adhesion contact using material with variable elastic modulus. *J Adhesion Sci Technol* 2010; 24(11–12): 1819–1830.
- [20] Barthel, E, and Perriot, A. Adhesive contact to a coated elastic substrate. *J Phys D: Appl Phys* 2007; 40(4): 1059–1067.
- [21] Dalmeida, R, Sharma, I, Upadhyay, C, et al. Contact of a rigid cylindrical punch with an adhesive elastic layer. *J Adhes* 2012; 88(1): 1–31.
- [22] Argatov, I, and Mishuris, G. Cylindrical lateral depth-sensing indentation of anisotropic elastic tissues: effects of adhesion and incompressibility. *J Adhes* 2018; 94: 583–596.
- [23] Keer, LM, and Miller, GR. Smooth indentation of finite layer. *J Eng Mech* 1983; 109(3): 706–717.
- [24] Sankar, BV, and Sun, CT. Indentation of a beam by a rigid cylinder. *Int J Solids Struct* 1983; 19(4): 293–303.
- [25] Kim, JH, Ahn, YJ, Jang, YH, et al. Contact problems involving beams. *Int J Solids Struct* 2014; 51(25–26): 4435–4439.
- [26] Punati, VS, Sharma, I, and Wahi, P. Indentation of adhesive beams. *Int J Solids Struct* 2018; 141: 137–157.
- [27] Sneddon, IN. *Fourier transforms*. New York: Dover Publications, 1995.
- [28] Rice, JR. A path independent integral and the approximate analysis of strain concentration by notches and cracks. *J Appl Mech* 1968; 35(2): 379–386.
- [29] Polyanin, A, and Manzhirov, A. *Handbook of integral equations*, 2nd edition. Boca Raton, FL: Chapman & Hall/CRC, 2008.
- [30] Kanninen, MF, and Popelar, CL. *Advanced fracture mechanics*. New York: Oxford University Press, 1985.
- [31] Chaudhury, MK, Weaver, T, Hui, C et al. Adhesive contact of cylindrical lens and a flat sheet. *J Appl Phys* 1996; 80(1): 30–37.
- [32] Johnston, ID, McCluskey, DK, Tan, CKL, et al. Mechanical characterization of bulk Sylgard 184 for microfluidics and microengineering. *J Micromech Microeng* 2014; 24(3): 035017.
- [33] Arul, EP, and Ghatak, A. Bioinspired design of a hierarchically structured adhesive. *Langmuir* 2008; 25(1): 611–617.
- [34] Chaudhury, MK, and Whitesides, GM. Direct measurement of interfacial interactions between semispherical lenses and flat sheets of poly(dimethylsiloxane) and their chemical derivatives. *Langmuir* 1991; 7(5): 1013–1025.
- [35] Timoshenko, SP, and Goodier, JN. *Theory of elasticity*. Singapore: McGraw-Hill, 1970.
- [36] Sadd, MH. *Elasticity: theory, applications, and numerics*. New Delhi: Elsevier India, 2005.
- [37] Press, WH, Teukolsky, SA, Vetterling, WT, et al. *Numerical recipes in C: the art of scientific computing*. New Delhi: Cambridge University Press India Pvt. Ltd., 1992.
- [38] Atkinson, EK. *The numerical solution of integral equations of the second kind*. Cambridge: Cambridge University Press, 1997.
- [39] Mason, JC, and Handscomb, DC. *Chebyshev polynomials*. Boca Raton, FL: Chapman & Hall/CRC, 2003.
- [40] Chatterjee, A. Lecture notes: an elementary continuation technique. <http://home.iitk.ac.in/~anindya/continuation.pdf>, 2002 (accessed 1 December 2016).
- [41] Muthukumar, T. Lecture notes: Sobolev spaces and applications. <http://home.iitk.ac.in/~tmk/courses/mth656/main.pdf>, 2016 (accessed 1 December 2016).

Appendix A Governing equations

In plane strain, the horizontal (u) and vertical (v) displacements of the (extended) elastic layer of Figure 1(b) are governed by

$$\frac{2(1-\nu)}{1-2\nu} \frac{\partial^2 u}{\partial x^2} + \frac{\partial^2 u}{\partial y^2} + \frac{1}{1-2\nu} \frac{\partial^2 v}{\partial x \partial y} = 0 \quad (24a)$$

and

$$\frac{\partial^2 v}{\partial x^2} + \frac{2(1-\nu)}{1-2\nu} \frac{\partial^2 v}{\partial y^2} + \frac{1}{1-2\nu} \frac{\partial^2 u}{\partial x \partial y} = 0, \quad (24b)$$

respectively [35, 36]. We now employ Fourier transforms [27]. In Fourier space the transformed horizontal and vertical displacements may be solved as, respectively,

$$U(\xi, y) = \{\kappa a_1 + \xi y (a_1 + ia_3)\} e^{\xi y} + \{\kappa b_1 - \xi y (b_1 - ib_3)\} e^{-\xi y} \quad (25)$$

and

$$V(\xi, y) = \{\kappa a_3 + i\xi y (a_1 + ia_3)\} e^{\xi y} + \{\kappa b_3 + i\xi y (b_1 - ib_3)\} e^{-\xi y}, \quad (26)$$

with

$$U(\xi, y) = \int_{-\infty}^{\infty} u(x, y) e^{i\xi x} dx, \quad V(\xi, y) = \int_{-\infty}^{\infty} v(x, y) e^{i\xi x} dx,$$

and a_1, a_3, b_1 and b_3 being unknown constants. These constants are found by applying boundary conditions

$$\sigma_{xy} = 0, \quad \sigma_{yy} = -P_c(x) \quad \text{on the top surface, that is at } y = 0, \quad (27a)$$

and

$$\sigma_{xy} = 0, \quad v = v_b(x) \quad \text{on the bottom surface, that is at } y = h, \quad (27b)$$

which in Fourier space become, respectively,

$$S_{\xi y} = 0, \quad S_{yy} = \bar{P}_c(\xi) \quad \text{at } y = 0, \quad (28a)$$

and

$$S_{\xi y} = 0, \quad V = \bar{v}_b(\xi) \quad \text{at } y = h, \quad (28b)$$

with

$$S_{\xi y} = \frac{E}{2(1+\nu)} \left(\frac{d}{dy} U - i\xi V \right),$$

$$S_{yy} = \frac{E}{(1+\nu)} \left\{ \frac{d}{dy} V + \frac{\nu}{1-2\nu} \left(-i\xi U + \frac{d}{dy} V \right) \right\},$$

$$\bar{P}_c(\xi) = \int_{-\infty}^{\infty} -P_c(x) e^{i\xi x} dx$$

and

$$\bar{v}_b(\xi) = \int_{-\infty}^{\infty} v_b(x) e^{i\xi x} dx.$$

With this, we find the vertical displacement of the top surface in Fourier space to be

$$V(\xi, 0) = -\frac{2\bar{P}_c(\xi)}{E^*} \frac{\sinh^2 \xi h}{\xi (\xi h + \sinh \xi h \cosh \xi h)} + \bar{v}_b(\xi) \frac{\sinh \xi h + \xi h \cosh \xi h}{\xi h + \sinh \xi h \cosh \xi h},$$

while the normal traction at the bottom layer in Fourier space is

$$S_{yy}(\xi, h) = \bar{P}_c(\xi) \frac{\sinh \xi h + \xi h \cosh \xi h}{\xi h + \sinh \xi h \cosh \xi h} + E^* \bar{v}_b(\xi) \frac{\xi}{2} \frac{\sinh^2 \xi h - \xi^2 h^2}{\xi h + \sinh \xi h \cosh \xi h},$$

where $E^* = E/(1 - \nu^2)$.

Employing the inverse Fourier transforms yields the vertical displacement of the layer's top surface ($y = 0$) and the normal traction acting on the layer's bottom surface ($y = h$) as, respectively,

$$v(x, 0) = -\frac{2}{\pi E^*} \int_0^\infty \bar{P}_c(\xi) K_1(\xi, x) d\xi + \frac{1}{\pi} \int_0^\infty \bar{v}_b(\xi) K_2(\xi, x) d\xi \quad (29)$$

and

$$\sigma_{yy}(x, h) = \frac{1}{\pi} \int_0^\infty \bar{P}_c(\xi) K_2(\xi, x) d\xi + \frac{E^*}{\pi} \int_0^\infty \bar{v}_b(\xi) K_3(\xi, x) \cos \xi x d\xi, \quad (30)$$

where

$$\bar{P}_c(\xi) = \int_{-\infty}^\infty -P_c(t) \cos \xi t dt \quad \text{and} \quad \bar{v}_b(\xi) = \int_{-\infty}^\infty v_b(t) \cos \xi t dt \quad (31)$$

are the Fourier transforms of the normal force $P_c(t)$ and the vertical displacement $v_b(t)$, while

$$K_1(\xi, x) = \frac{\sinh^2 \xi h}{\xi (\xi h + \sinh \xi h \cosh \xi h)} \cos \xi x,$$

$$K_2(\xi, x) = \frac{\sinh \xi h + \xi h \cosh \xi h}{\xi h + \sinh \xi h \cosh \xi h} \cos \xi x$$

and

$$K_3(\xi, x) = \frac{\xi}{2} \cdot \frac{\sinh^2 \xi h - \xi^2 h^2}{\xi h + \sinh \xi h \cosh \xi h} \cos \xi x.$$

We expand equations (29) and (30) by employing definitions of \bar{P}_c and \bar{v}_b to obtain:

$$v(x, 0) = \frac{2}{\pi E^*} \int_0^\infty \int_{-\infty}^\infty P_c(t) \cos \xi t dt K_1(\xi, x) d\xi + \frac{1}{\pi} \int_0^\infty \int_{-\infty}^\infty v_b(t) \cos \xi t dt K_2(\xi, x) d\xi \quad (32)$$

and

$$\sigma_{yy}(x, h) = \frac{1}{\pi} \int_0^\infty \int_{-\infty}^\infty -P_c(t) \cos \xi t dt K_2(\xi, x) d\xi + \frac{E^*}{\pi} \int_0^\infty \int_{-\infty}^\infty v_b(t) \cos \xi t dt K_3(\xi, x) d\xi. \quad (33)$$

In equation (33), the second integral is singular at $\xi \rightarrow \infty$. This singularity is eliminated by integrating twice by parts, to find

$$\sigma_{yy}(x, h) = \frac{1}{\pi} \int_0^\infty \int_{-\infty}^\infty -P_c(t) \cos \xi t dt K_2(\xi, x) d\xi - \frac{E^*}{\pi} \int_0^\infty \int_{-\infty}^\infty \kappa_b(t) \cos \xi t dt \frac{1}{\xi^2} K_3(\xi, x) d\xi, \quad (34)$$

where $\kappa_b(t) = d^2 v_b/dt^2$ is the curvature of the layer's bottom surface. Equations (32) and (34) lead to the governing equations (2) and (3) of the main text, after non-dimensionalization and imposing the traction and kinematic conditions on the top and bottom surfaces of the layer.

Appendix B Displacement of the layer's bottom surface

We approximate the vertical displacement of the bottom surface in a layer that is clamped at its ends as

$$v_b^c(\chi) = d_0^c + \sum_{n=1}^M d_n^c \cos(n\pi\chi). \quad (35)$$

The above displacement field is symmetric in χ , that is $v_b^c(\chi) = v_b^c(-\chi)$. The slope conditions at the ends, that is $dv_b^c/d\chi = 0$ at $\chi = \pm 1$, are automatically satisfied. We find the unknown coefficient d_0^c in equation (35) by invoking $v_b^c(\pm 1) = 0$, to obtain

$$d_0^c = \sum_{n=1}^M d_n^c (-1)^{n+1}. \quad (36)$$

Combining equations (35) and (36) yields

$$v_b^c(\chi) = \sum_{n=1}^M d_n^c [(-1)^{n+1} + \cos(n\pi\chi)]. \quad (37)$$

Differentiating the above twice with respect to χ provides, finally,

$$\kappa_b^c(\chi) = -\pi^2 \sum_{n=1}^M d_n^c n^2 \cos(n\pi\chi). \quad (38)$$

For a simply supported elastic layer, we approximate the vertical displacement of the bottom surface within $-1 \leq \chi \leq 1$ as

$$v_b^s(\chi) = d_0^s + \sum_{n=1}^M d_{2n-1}^s \sin\left\{\frac{(2n-1)\pi(\chi+1)}{2}\right\}. \quad (39)$$

Note that the above is symmetric about $\chi = 0$, as it should be. The above displacement field also satisfies $d^2v_b^s/d\chi^2 = 0$ at $\chi = \pm 1$, as appropriate for a simply supported layer. Satisfying $v^s(\pm 1) = 0$ yields the unknown constant $d_0^s = 0$. Hence, $v_b^s(\chi)$ becomes

$$v_b^s(\chi) = \sum_{n=1}^M d_{2n-1}^s (-1)^{n-1} \cos\left\{\frac{(2n-1)\pi\chi}{2}\right\}. \quad (40)$$

Differentiating the above twice we obtain the curvature $\kappa_b^s(\chi)$ as

$$\begin{aligned} \kappa_b^s(\chi) = & - \sum_{n=1}^M d_{2n-1}^s (-1)^{n-1} \left\{\frac{(2n-1)\pi}{2}\right\}^2 \\ & \cos\left\{\frac{(2n-1)\pi\chi}{2}\right\}, \quad -1 \leq \chi \leq 1. \end{aligned} \quad (41)$$

Calculating the slope at the ends of the layer yields

$$\left.\frac{dv_b^s(\chi)}{d\chi}\right|_{\chi=1} = - \sum_{n=1}^M d_{2n-1}^s \frac{(2n-1)\pi}{2}. \quad (42)$$

Finally, finding the displacement in $1 < \chi < \infty$, after extending the layer along its slope at the end supports (see Figure 1(b)), we obtain

$$v_b^s(\chi) = \left.\frac{dv_b^s(\chi)}{d\chi}\right|_{\chi=1} (\chi - 1). \quad (43)$$

Appendix C Discretization and numerical algorithm

Substituting equations (14) and (15) into the integral equations (2) and (3) yields, respectively,

$$\Delta - \frac{1}{2}x^2A^2 = \frac{8m}{3\pi} \sum_{n=0}^N b_{2n} \mathcal{J}_{2n}^t(x) - \frac{8\lambda A}{3\pi} \mathcal{J}^t(x) + \frac{1}{\pi\gamma} \sum_{n=1}^M d_n \mathcal{Q}_n^t(x) \quad (44)$$

and

$$0 = \frac{8m}{3\pi} \sum_{n=0}^N b_{2n} \mathcal{J}_{2n}^b(\chi) - \frac{8\lambda A}{3\pi} \mathcal{J}^b(\chi) + \frac{\hat{\gamma}}{\pi} \sum_{n=1}^M d_n \mathcal{Q}_n^b(\chi), \quad (45)$$

where

$$\begin{aligned} \mathcal{J}_{2n}^t(x) &= \int_0^\infty \alpha_{2n} \left(\frac{\omega}{h} \right) K_1^t \left(\frac{\omega}{h}, x \right) d\omega, \\ \mathcal{J}^t(x) &= \int_0^\infty \frac{h}{\omega} \sin \left(\frac{\omega c}{h} \right) K_1^t \left(\frac{\omega}{h}, x \right) d\omega, \\ \mathcal{Q}_n^t(x) &= \int_0^\infty \bar{\beta}_n \left(\frac{\omega}{\gamma} \right) K_2^t \left(\frac{\omega}{h}, x \right) d\omega, \\ \mathcal{Q}_n^b(\chi) &= \int_0^\infty \bar{\kappa}_n \left(\frac{\omega}{\gamma} \right) K_2^b \left(\frac{\omega}{\gamma}, \chi \right) d\omega, \\ \mathcal{J}_{2n}^b(\chi) &= \int_0^\infty \alpha_{2n} \left(\frac{\omega}{h} \right) K_1^b \left(\frac{\omega}{\gamma}, \chi \right) d\omega \\ \text{and} \quad \mathcal{J}^b(\chi) &= \int_0^\infty \frac{h}{\omega} \sin \left(\frac{\omega c}{h} \right) K_1^b \left(\frac{\omega}{\gamma}, \chi \right) d\omega \end{aligned} \quad (46)$$

are known in terms of the functions $\bar{\beta}_n$ and $\bar{\kappa}_n$ that are obtained from the displacement of the bottom surface in Appendix E, while

$$\alpha_{2n}(s) = \int_{-1}^1 \frac{1}{\sqrt{(1-\tau^2)}} T_{2n}(\tau) \cos(s\tau) d\tau, \quad (47)$$

which are computed in closed form in Appendix F. The integrals in equation (46) are computed at any x or χ through the Clenshaw–Curtis quadrature [37]. We now solve equations (44) and (45) through the *collocation technique* [38].

In the collocation method, equations (44) and (45) are required to hold exactly at, respectively, $N + 1$ and M *collocation points*. The collocation points for equations (44) and (45) are selected to be, respectively,

$$x_i = \cos \left\{ \frac{(2i-1)\pi}{2(N+1)} \right\} \text{ for } i = 1, \dots, N+1,$$

and

$$\chi_k = \frac{k-1}{M} \text{ for } k = 1, \dots, M.$$

Here, x_i are the $N + 1$ zeros of the Chebyshev polynomial $T_{2N+2}(x_i)$ [39], while χ_k are equally spaced points lying between 0 and 1. At these collocation points, equations (44) and (45) become, respectively, equations (16) and (17). In addition to these, we also have the end condition (18) and energy balance (19). The $N + M + 3$

nonlinear algebraic equations (16)–(19) are to be solved for $N + M + 3$ unknowns b_{2n} , d_n , Δ and c . This is done through the following algorithm:

Step 1: For a given contact area A , we make an initial guess for c .

Step 2: We then write equations (16) and (17) in matrix notation as

$$\Delta \underline{e} - \underline{f} - \underline{\lambda} = \underline{R} \underline{a}, \quad (48)$$

where

$$\begin{aligned} \underline{e} &= [\underline{e}^t, \underline{e}^b]^T; \underline{f} = [\underline{f}^t, \underline{f}^b]^T; \underline{\lambda} = [\underline{\lambda}^t, \underline{\lambda}^b]^T; \\ \underline{a} &= [\underline{a}^t, \underline{a}^b]^T; \underline{R} = \begin{bmatrix} \underline{\mathcal{J}}^t & \underline{\mathcal{Q}}^t \\ \underline{\mathcal{J}}^b & \underline{\mathcal{Q}}^b \end{bmatrix}, \end{aligned} \quad (49)$$

with

$$\begin{aligned} a_i^t &= b_{2i-2}; \quad a_k^b = d_k; \quad e_i^t = 1; \quad e_k^b = 0; \\ f_i^t &= \frac{x_i^2 A^2}{2}; \quad f_k^b = 0; \quad \lambda_i^t = -\frac{8\lambda A}{3\pi} \mathcal{J}^t(x_i); \\ \lambda_k^b &= -\frac{8\lambda A}{3\pi} \mathcal{J}^b(\chi_k); \quad \mathcal{J}_{ij}^t = \frac{8m}{3\pi} \mathcal{J}_{2j-2}^t(x_i); \\ \mathcal{Q}_{ir}^t &= \frac{1}{\pi\gamma} \mathcal{Q}_r^t(x_i); \quad \mathcal{J}_{kj}^b = \frac{8m}{3\pi} \mathcal{J}_{2j-2}^b(\chi_k); \\ \mathcal{Q}_{ir}^b &= \frac{\gamma}{\pi} \mathcal{Q}_r^b(\chi_k), \end{aligned} \quad (50)$$

for $i, j = 1, 2, \dots, N + 1$ and $k, r = 1, 2, \dots, M$. Thus, $\underline{e}, \underline{f}, \underline{\lambda}, \underline{a}$ are column vectors of size $N + M + 1$, and \underline{R} is a square matrix of size $N + M + 1$.

Step 3: The column vector \underline{a} consists of the coefficients occurring in expressions (14) for the contact pressure and (15) for the displacement. We invert equation (48) to find \underline{a} in terms of Δ :

$$\underline{a} = \Delta \underline{E} - \underline{F} - \underline{\Lambda}, \quad (51)$$

where

$$\underline{E} = \underline{R}^{-1} \underline{e}, \quad \underline{F} = \underline{R}^{-1} \underline{f} \quad \text{and} \quad \underline{\Lambda} = \underline{R}^{-1} \underline{\lambda}.$$

Step 4: Employing the end condition (18) for the contact pressure, we obtain the punch's displacement

$$\Delta = \frac{p_0 + \sum_{i=1}^{N+1} F_i + \sum_{i=1}^{N+1} \Lambda_i}{\sum_{i=1}^{N+1} E_i}, \quad (52)$$

where

$$p_0 = \begin{cases} 0 & \text{if there is no adhesion or an adhesive zone is present,} \\ -\sqrt{6A}/2\pi m & \text{if the JKR approximation is invoked; see equation (20).} \end{cases}$$

Step 5: Once Δ is known, we evaluate \underline{a} from equation (51) through

$$\underline{a} = \left(\frac{p_0 + \sum_{i=1}^{N+1} F_i + \sum_{i=1}^{N+1} \Lambda_i}{\sum_{i=1}^{N+1} E_i} \right) \underline{E} - \underline{F} - \underline{\Lambda}. \quad (53)$$

Step 6: Utilizing Δ and \underline{a} , we calculate the displacement of the layer's top surface at c and check whether equation (19) holds. If not, then we update c employing the Newton–Raphson method [40]. Steps 1–6 are repeated

until equation (19) is satisfied. Steps 1 and 6 are required only when we employ an adhesive zone. When the Hertzian or JKR approximations are invoked, we skip Steps 1 and 6.

Step 7: We finally proceed to find the contact pressure distribution $\varphi(x)$ and the total load \bar{P} from equations (14) and (21), respectively.

Appendix D Non-adhesive contact

Finite element (FE) computations are carried out for clamped and simply supported elastic layers for adhesionless contact. These are employed to validate our semi-analytical results.

The FE model is prepared in ABAQUS as follows. The finite linear elastic layer of Young's modulus $E = 2000$ MPa, Poisson's ratio $\nu = 0.3$, thickness $h = 4$ mm and half-span $l = 40$ mm is modelled. The rigid cylindrical punch is modelled as a much stiffer elastic material with Young's modulus $E_p = 2 \times 10^8$ MPa and radius $R = 225$ mm. Plane-strain elements are considered both for the layer and the punch. A concentrated load is applied on the punch. Computations provide the contact pressure φ , contact area A , punch's displacement Δ and the displacement v_b of the layer's bottom surface. In these computations the 'nlin-geom' option in ABAQUS was not selected as we are comparing with the linearized theory of Section 2.

We will employ the following non-dimensional variables to compare with FE computations and available literature:

$$\begin{aligned} \hat{A} &= \frac{a}{l}, & \hat{\varphi}(x) &= \frac{aRl}{Kh^3} p(x), & \phi(x) &= \frac{ap(x)}{P}, \\ \hat{P} &= \frac{PRl}{Kh^3} & \text{and} & & \hat{\Delta} &= \frac{\delta R}{l^2}. \end{aligned} \quad (54)$$

Figure 14 plots $\hat{\varphi}(x)$ and $\phi(x)$ obtained for both clamped and simply supported elastic layers. These pressure profiles are plotted at different values of a/h by varying the contact area a . Comparing Figures 14 (a) and (c) we find that, at the same a/h , the contact pressure $\hat{\varphi}$ in a simply supported layer is lower than that in a clamped layer. However, this difference is suppressed when we plot $ap(x)/P$; see Figures 14(b) and 14(d).

We observe a close match between our predictions and FE simulations for all a/h , except for a small deviation between the two at $a/h = 2.5$ in the case of simply supported layers. This may be due to the shear-free boundary condition at the top and bottom surface of the layer that was employed in the theoretical model but is not imposed in the FE model. Loss of contact at deeper indentation is predicted by both theory and FE computations. Theory predicts contact loss when $a/h \gtrsim 2.5$ for clamped layers and when $a/h \gtrsim 2.5$ for simply supported layers. The FE results agree with the former, but find contact loss when $a/h \gtrsim 2.25$ for the latter case.

Next, in Figure 15 we compare our results for contact pressures $\phi(x)$ with those of Keer and Miller [23]. We find an extremely close match between the two until $a/h \approx 2$. Beyond that, we find negative pressures – indicating contact loss – at the centre of the contact patch, whereas Keer and Miller [23] do not. Earlier formulations of Keer and Miller [23] – also Sankar and Sun [24] which we discuss below – did *not* predict contact loss. Figure 15 reaffirms our earlier observation that contact pressures of clamped and simply supported layers do *not* vary much, when scaled as $ap(x)/P$.

Finally, in Figure 16 we plot the variation of the contact area \hat{A} with the total load \hat{P} on the punch and the punch's displacement $\hat{\Delta}$. We also compare with FE computations and results of Sankar and Sun [25]. This process is repeated for the variation of $\hat{\Delta}$ with \hat{P} in Figure 17. We find a close match of our theoretical predictions with FE computations and the earlier results of Sankar and Sun [24].

Appendix E Evaluating $\bar{v}_b(\omega/\gamma)$ and $\bar{\kappa}_b(\omega/\gamma)$

The Fourier transforms of v_b and κ_b cannot always be computed as these functions may not be well-behaved at infinity for the extended layer. Indeed, in a simply supported layer, the displacement grows linearly to infinity outside the supports. To address this we employ mollifiers to regularize the Fourier transforms $\bar{v}_b(\omega/\gamma)$ and

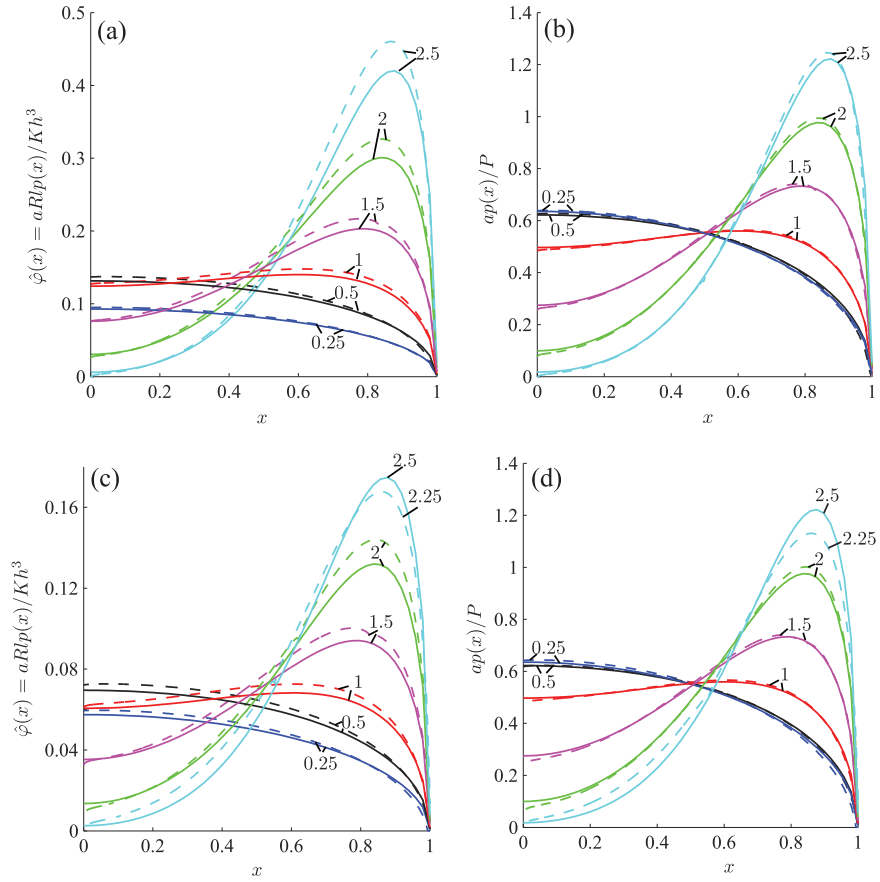


Figure 14. The non-dimensional contact pressures $\hat{\phi}(x)$ and $\phi(x)$ during the non-adhesive indentation of clamped (top row) and simply supported (bottom row) layers. We set $h = 4$ mm and $l = 40$ mm. Several contact areas a are investigated by varying a/h as noted next to their corresponding curves. The solid lines are results obtained from the semi-analytical procedure of Section 2, while dashed lines represent finite element computations.

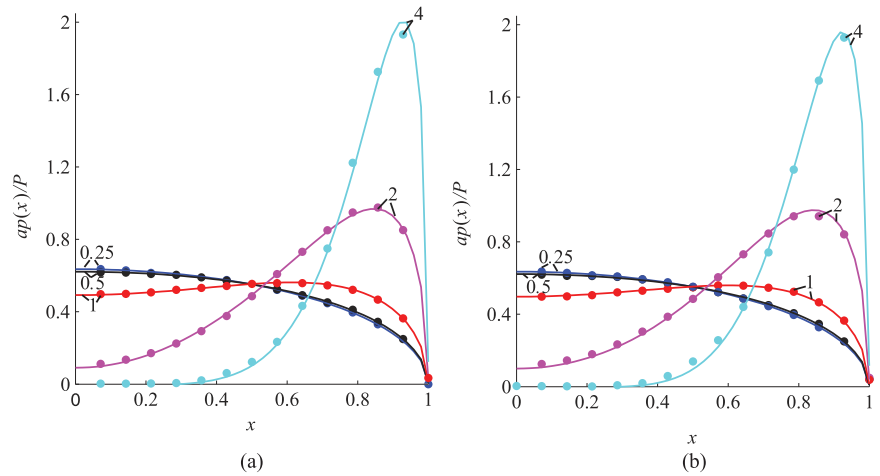


Figure 15. The non-dimensional contact pressures $\phi(x)$ during the non-adhesive indentation of (a) a clamped layer and (b) a simply supported layer. The slenderness ratio of the layer $l/h = 10$. Several contact areas a are investigated by varying a/h as noted next to their corresponding curves. The solid lines are results obtained from the semi-analytical procedure of Section 2. Dots represent the predictions of Keer and Miller [23].

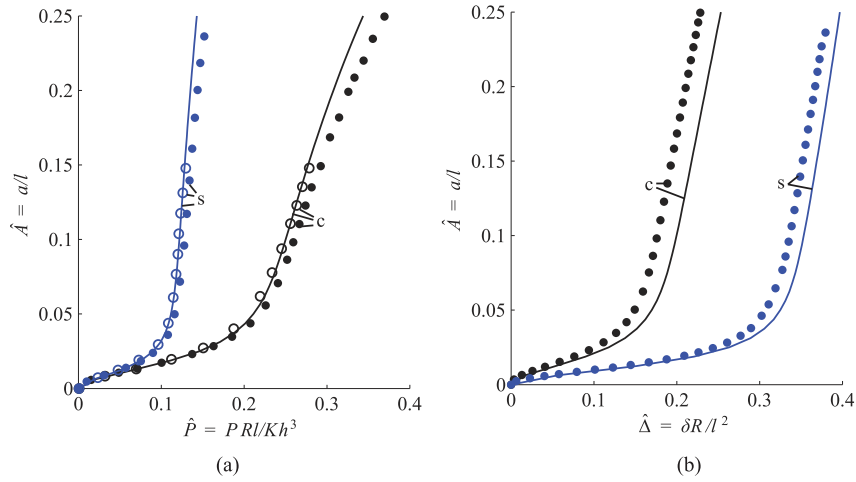


Figure 16. Non-adhesive contact of clamped ('c') and simply supported ('s') layers. The contact area \hat{A} is plotted as a function of (a) the total load \hat{P} acting on the punch and (b) the punch's displacement $\hat{\Delta}$. The layer's slenderness ratio $l/h=10$. Solid lines are results obtained from the semi-analytical procedure of Section 2. Filled circles correspond to our finite element simulations. Predictions of Sankar and Sun [24] are shown by open circles, when available.

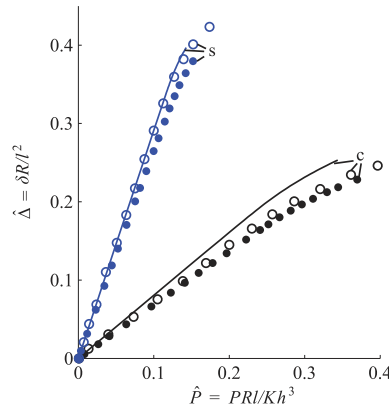


Figure 17. Non-adhesive contact of clamped ('c') and simply supported ('s') layers. The displacement $\hat{\Delta}$ of the punch is shown as a function of the total load \hat{P} . See also the caption of Figure 16.

$\bar{\kappa}_b(\omega/\gamma)$ as follows:

$$\bar{v}_b\left(\frac{\omega}{\gamma}\right) = \int_{-\infty}^{\infty} v_b(\tau) W(\tau) \cos\left(\frac{\omega\tau}{\gamma}\right) d\tau \quad (55)$$

and

$$\bar{\kappa}_b\left(\frac{\omega}{\gamma}\right) = \int_{-\infty}^{\infty} \frac{d^2}{d\tau^2} [v_b(\tau) W(\tau)] \cos\left(\frac{\omega\tau}{\gamma}\right) d\tau, \quad (56)$$

where the mollifier $W(\tau)$ is defined [41] as

$$W(\tau) = \begin{cases} 1 & \text{for } |\tau| \leq |l_1|, \\ w_2(\tau) & \text{for } |l_1| < |\tau| < |l_2|, \\ 0 & \text{for } |\tau| \geq |l_2|, \end{cases} \quad (57a)$$

with

$$w_2(\tau) = \frac{\exp\{-1/(l_2 - \tau)^2\}}{\exp\{-1/(l_2 - \tau)^2\} + \exp\{-1/(\tau - l_1)^2\}}, \quad (57b)$$

and l_1 and l_2 locate points on the layer that are far away from the ends with $l_2 > l_1 \gg 1$. The mollifier $W(\tau)$ is infinitely differentiable, and alters the displacement far from the layer's ends and makes it integrable. Because the layer's displacement is modified far from the supports, we do not expect any impact on the indentation process in keeping with St. Venant's principle [36].

For a clamped layer we obtain from equations (55) and (56)

$$\bar{v}_b^c\left(\frac{\omega}{\gamma}\right) = \sum_{n=1}^M d_n^c \bar{\beta}_n^c\left(\frac{\omega}{\gamma}\right) \quad \text{and} \quad \bar{k}_b^c\left(\frac{\omega}{\gamma}\right) = \sum_{n=1}^M d_n^c \bar{\kappa}_n^c\left(\frac{\omega}{\gamma}\right), \quad (58)$$

where

$$\bar{\beta}_n^c\left(\frac{\omega}{\gamma}\right) = \frac{2\gamma(-1)^{n+1} \sin(\omega/\gamma)}{\omega} + \frac{2\omega\gamma(-1)^{n+1} \sin(\omega/\gamma)}{n^2\pi^2\gamma^2 - \omega^2} \quad (59)$$

$$\text{and} \quad \bar{\kappa}_n^c\left(\frac{\omega}{\gamma}\right) = -n^2\pi^2 \frac{2\omega\gamma(-1)^{n+1} \sin(\omega/\gamma)}{n^2\pi^2\gamma^2 - \omega^2}. \quad (60)$$

For a simply supported layer we find from equations (55) and (56)

$$\bar{v}_b^s\left(\frac{\omega}{\gamma}\right) = \sum_{n=1}^M \tilde{d}_n^s \bar{\beta}_n^s\left(\frac{\omega}{\gamma}\right) \quad \text{and} \quad \bar{k}_b^s\left(\frac{\omega}{\gamma}\right) = \sum_{n=1}^M \tilde{d}_n^s \bar{\kappa}_n^s\left(\frac{\omega}{\gamma}\right), \quad (61)$$

where $\tilde{d}_n^s = d_{2n-1}^s$,

$$\begin{aligned} \bar{\beta}_n^s\left(\frac{\omega}{\gamma}\right) &= \int_{-1}^1 (-1)^{n-1} \cos\left\{\frac{(2n-1)\pi\tau}{2}\right\} \cos\left(\frac{\omega\tau}{\gamma}\right) d\tau \\ &\quad - (2n-1)\pi \int_1^{l_2} (\tau-1) W(\tau) \cos\left(\frac{\omega\tau}{\gamma}\right) d\tau \end{aligned}$$

$$\begin{aligned} \text{and} \quad \bar{\kappa}_n^s\left(\frac{\omega}{\gamma}\right) &= -\left\{\frac{(2n-1)\pi}{2}\right\}^2 \int_{-1}^1 (-1)^{n-1} \cos\left\{\frac{(2n-1)\pi\tau}{2}\right\} \cos\left(\frac{\omega\tau}{\gamma}\right) d\tau \\ &\quad - 2(2n-1)\pi \int_{l_1}^{l_2} \frac{dw_2(\tau)}{d\tau} \cos\left(\frac{\omega\tau}{\gamma}\right) d\tau \\ &\quad - (2n-1)\pi \int_{l_1}^{l_2} (\tau-1) \frac{d^2w_2(\tau)}{d\tau^2} \cos\left(\frac{\omega\tau}{\gamma}\right) d\tau. \end{aligned} \quad (62)$$

Finally, employing equations (58) and (61), we may write

$$\bar{v}_b\left(\frac{\omega}{\gamma}\right) = \sum_{n=1}^M d_n \bar{\beta}_n\left(\frac{\omega}{\gamma}\right) \quad \text{and} \quad \bar{k}_b\left(\frac{\omega}{\gamma}\right) = \sum_{n=1}^M d_n \bar{\kappa}_n\left(\frac{\omega}{\gamma}\right), \quad (63)$$

where $\bar{\beta}_n$ and $\bar{\kappa}_n$ are given by equations (60) and (62) for clamped and simply supported layers, respectively.

Appendix F Evaluating $\bar{\varphi}(\omega/h)$ and $\bar{\varphi}_0(\omega/h)$

When the series expansion (equation (14) in the main text) is employed to compute $\bar{\varphi}$ and $\bar{\varphi}_0$, we obtain

$$\bar{\varphi}\left(\frac{\omega}{h}\right) = \frac{\lambda Ah}{m} \frac{\sin(\omega/h)}{\omega} - \sum_{n=0}^N b_{2n} \alpha_{2n}\left(\frac{\omega}{h}\right)$$

and

$$\bar{\varphi}_0\left(\frac{\omega}{h}\right) = \frac{h}{\omega} \left\{ -\sin\left(\frac{\omega}{h}\right) + \sin\left(\frac{\omega c}{h}\right) \right\}, \quad (64)$$

where

$$\alpha_{2n}\left(\frac{\omega}{h}\right) = \int_{-1}^1 \frac{1}{\sqrt{1-\tau^2}} T_{2n}(\tau) \cos\left(\frac{\omega\tau}{h}\right) d\tau. \quad (65)$$

We now compute the above integrals explicitly. First, consider odd n . For this, the integrand is an odd function so that

$$\alpha_{2n-1}(\zeta) = 0, \quad (66)$$

where $\zeta = \omega/h$. Next, evaluating equation (65) for even n , we obtain the first few α_n as

$$\begin{aligned} \alpha_0(\zeta) &= \pi J(0, \zeta), \\ \alpha_2(\zeta) &= \pi J(0, \zeta) - \frac{2\pi J(1, \zeta)}{\zeta}, \\ \alpha_4(\zeta) &= \pi J(0, \zeta) - \frac{8\pi J(1, \zeta)}{\zeta} - \frac{24\pi J(0, \zeta)}{\zeta^2} + \frac{48\pi J(1, \zeta)}{\zeta^3}, \\ \text{and} \quad \alpha_6(\zeta) &= \pi J(0, \zeta) - \frac{18\pi J(1, \zeta)}{\zeta} - \frac{144\pi J(0, \zeta)}{\zeta^2} + \frac{768\pi J(1, \zeta)}{\zeta^3} \\ &\quad + \frac{1920\pi J(0, \zeta)}{\zeta^4} - \frac{3840\pi J(1, \zeta)}{\zeta^5}, \end{aligned} \quad (67)$$

where $J(n, \xi)$ are Bessel's functions of the first kind of order n [29]. Employing the recurrence relation [29],

$$J(n+1, \zeta) = \frac{2n}{\zeta} J(n, \zeta) - J(n-1, \zeta),$$

we rewrite equation (67) as

$$\alpha_2(\zeta) = -\pi J(2, \zeta), \quad \alpha_4(\zeta) = \pi J(4, \zeta) \quad \text{and} \quad \alpha_6(\zeta) = -\pi J(6, \zeta).$$

In general, it is possible to show that

$$\alpha_{2n}(\zeta) = (-1)^n \pi J(2n, \zeta). \quad (68)$$

Finally, substituting $\zeta = \omega/h$ in the above yields

$$\alpha_{2n}\left(\frac{\omega}{h}\right) = (-1)^n \pi J\left(2n, \frac{\omega}{h}\right). \quad (69)$$